Chinese Chemical Letters 35 (2024) 108475

Contents lists available at ScienceDirect

Chinese Chemical Letters

journal homepage: www.elsevier.com/locate/cclet

Plasmonic Ag nanoparticles decorated MIL-101(Fe) for enhanced photocatalytic degradation of bisphenol A with peroxymonosulfate under visible-light irradiation

Yan Gong[a], Yu Ding[a], Qi Tang[a], Fei Lian[a,*], Chun Bai[a], Ruiyi Xie[a], Haijiao Xie[b], Xu Zhao[c,*]

[a] School of Energy and Environmental Engineering, Hebei University of Technology, Tianjin 300401, China
[b] Hangzhou Yanqu Information Technology Co., Ltd., Hangzhou 310003, China
[c] Key Laboratory of Drinking Water Science and Technology, Research Center for Eco-Environmental Sciences, Chinese Academy of Sciences, Beijing 100085, China

ARTICLE INFO

Article history:
Received 23 December 2022
Revised 28 March 2023
Accepted 18 April 2023
Available online 18 April 2023

Keywords:
Photocatalysis
MOF
Peroxymonosulfate
Plasmonic Ag
BPA

ABSTRACT

Photocatalytic activation of peroxymonosulfate (PMS) has garnered a lot of interest in the field of wastewater treatment. Herein, a plasmonic Ag nanoparticles decorated MIL-101(Fe) hybrid was synthesized through a photodeposition process. Upon light irradiation, the Ag/MIL-101(Fe) exhibit reinforced photocatalytic activities for elimination of bisphenol A (BPA) with PMS. The optimized 2.0% Ag/MIL-101(Fe) composite presented the highest photocatalytic activity with kinetic constant k of 0.102 min^{-1}, which was about 10-fold of the pristine MIL-101(Fe). Loading of plasmonic Ag into MIL-101(Fe) boosts photoinduced carrier separation and accelerates PMS activation to generate strong oxidative radicals. Photoelectrochemical tests and multiple spectroscopic studies confirmed the promoted charge carrier separation and transfer capability of Ag/MIL-101(Fe). Combining the results of radical trapping experiments and electron spin resonance (ESR), the formed $SO_4^{\bullet-}$, $^{\bullet}OH$, $^{\bullet}O_2^-$ and $^1O_2$ had a significant role in the photocatalytic process. According to intermediate study, the degradation pathway was studied, and the possible mechanism was proposed.

Bisphenol A, a typical environmental endocrine disruptor (EEDs), has been frequently applied in the production of chemical raw materials [1]. It has raised serious concerns associated with the detrimental effects on causing nervous system disorder, low immunity and inducing complications such as tumors, which threaten the ecology and human being [2]. BPA has strong chemical stability, making it challenging to completely degrade for the commercial treatment process. Thus, it is a burning issue to explore a valid method to eliminate BPA from water [3]. In recent, advanced treatment technology based on the activated persulfate is regarded as a very effective way to remove BPA by the advantages of powerful oxidation. The peroxydisulfate (PDS) or peroxymonosulfate (PMS) can be triggered to generate $SO_4^{\bullet-}$ by means of ultraviolet light [4], electrochemical [5], alkali [6], ozone [7] and ultrasonic [8]. However, these methods are often inefficient, high-energy consumption. It is still essential to explore new methods to high-efficiency activate PMS.

Recently, photocatalytic activation of PMS has fascinated immense attention in removal refractory organics of waste water [9,10]. The efficient reductive photogenerated electrons originated from excited semiconductors can easily react with PMS to produced $SO_4^{\bullet-}$. Benefit from the high specific surface, adjustable porosity and modularity, metal-organic frameworks (MOFs) have drawn attention for catalysis [11], gas storage [12], adsorption [13] and separation [14]. Previous works revealed that the Fe-based MOF semiconductors showed a certain photocatalytic capability for PMS activation for water treatment [15]. However, the sluggish photogenerated carrier separation and moderate PMS activation greatly hinder the catalytic performance of bare Fe-based MOFs. Researchers have adopted many methods to improve the catalytic performance. To date, some progress has been made. For instance, Li *et al.* [16] reported a new quinone modified Fe-MOF, which promoted BPA degradation by PDS activation with the removal rate of 97.7%. Alternatively, a unique PDINH/MIL-88(Fe) composite has been created and exhibited excellent photocatalytic PDS activation for chloroquine phosphate degradation [17]. Jiang *et al.* [18] devised a $^1O_2$ dominated bacterial inactivation technique that effectively inactivates Gram-negative *Escherichia coli* in water utilizing CuS modified MIL-101(Fe) to activate PMS. It

* Corresponding authors.
E-mail addresses: lianfei2000@126.com (F. Lian), zhaoxu@rcees.ac.cn (X. Zhao).

https://doi.org/10.1016/j.cclet.2023.108475
1001-8417/

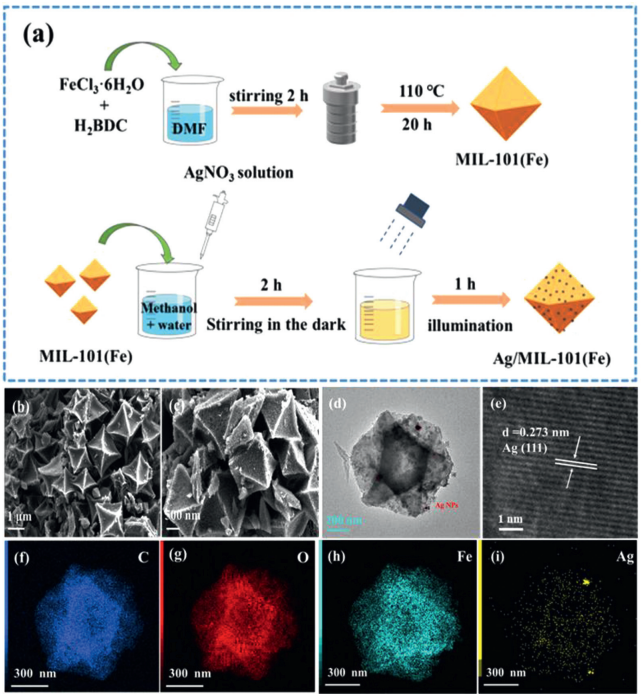

Fig. 1. (a) Schematic of the preparation of Ag/MIL-101(Fe); (b, c) SEM image of MIL-101(Fe) and Ag/MIL-101(Fe); (d) TEM image of Ag/MIL-101(Fe); (e) HRTEM of Ag/MIL-101(Fe); (f-i) EDX mapping images of Ag/MIL-101(Fe).

has been demonstrated that integration of plasmonic metals into photocatalysis is an advisable strategy for improving photocatalytic performance [19,20]. Originating from coherent oscillations of delocalized electrons of nanostructured metal by the electromagnetic field of incident light, the metals (such as Ag, Au) possess strong visible-light adsorption ability by the surface plasmon resonance (SPR). Recent studies proved that loading of SPR metals into semiconductor can boost photogenerated charge carrier separation and extend light response range [21]. Thus, the introduction of plasmonic metal Ag into Fe-MOF may have the following advantage: (i) Enhancing utilization of sunlight of Fe-MOF; (ii) preventing the recombination of photo-generated carriers; (iii) promoting PMS activation by the hot electrons generated from Ag NPs. In addition, Ag as transition metal can also trigger PMS activation.

Bearing these considerations in mind, a simple photodeposition method was employed to synthesize Ag/MIL-101(Fe) composites with different Ag content as shown in Text S1 (Supporting information) and Fig. 1a. As illustrated in SEM of Figs. 1b and c, both the prepared MIL-101(Fe) and Ag/MIL-101(Fe) composite were composed of octahedral structure with a uniform size of around 1 μm. TEM image (Fig. 1d) of composite indicated that the morphology of composite was similar with pristine MIL-101(Fe), and some nanoparticles were distinctly observed. From Fig. 1e, HRTEM image further revealed that the interplanar distances of 0.273 nm matched well with the standard (111) plane of Ag [22,23], which confirmed the existence of Ag nanoparticles (NPs). Moreover, the elemental mapping images in Figs. 1f-i further demonstrated the uniformly distributed of Ag over MIL-101(Fe) and the close contact of two components. This is beneficial to the effective transfer of photoinduced charge carrier at the interface. The above results indicated that Ag NPs have been successfully deposited on MIL-101(Fe).

The XRD patterns of catalysts are showed in Fig. 2a. For bare MIL-101(Fe), several peaks appeared in 9°∼22° are assigned to MIL-101(Fe) [24–26]. The diffraction peak positions of Ag/MIL-101(Fe) composite are almost the same as MIL-101(Fe), implying that the phase structure of host MIL-101(Fe) lattice did not change after Ag loading. Notably, the diffraction peaks belonged to Ag are less distinct, which might result from the relatively low Ag content. From the FT-IR spectra (Fig. 2b) of pristine MIL-101(Fe), two bands at 1591 and 1391 cm^{-1} corresponded to stretching vibration of carboxy groups. The band located at 749 cm^{-1} was assigned to bending vibration of C–H in benzene ring, and the band at 551 cm^{-1} belonged to Fe-O in MIL-101(Fe) [27,28]. For Ag/MIL-101(Fe), the bands position was as same as the pristine MIL-101(Fe), proving no altering of the chemical structure of MIL-101(Fe) after Ag loading. Moreover, as depicted in Fig. 2c of Raman spectra, the bands at range from 630 cm^{-1} to 1610 cm^{-1} belonging to the fingerprint information of benzene ring can be observed [29]. These peaks are assigned to the ligand terephthalic acid [30]. Significantly, compared to pristine MIL-101(Fe), the peak intensities of Ag/MIL-101(Fe) composite are obviously stronger, which may arise from the surface enhanced plasmon scattering of Ag nanoparticles [31].

As depicted in Fig. 2d, the absorption edge of all samples located at visible-light range, demonstrating the visible-light responses property. Obviously, Ag/MIL-101(Fe) composites exhibit enhanced absorption in whole visible light region, implying that Ag loading can broaden light response range of MIL-101(Fe). This may result from the characteristic SPR adsorption of metallic silver nanoparticles. In addition, from Fig. 2e of the Tauc plot, the band gaps were estimated to be 2.55 and 2.7 eV for Ag/MIL-101(Fe) and MIL-101(Fe), the smaller band gap also implied the extending light response range of the composite. These results indicate that introduction of Ag is beneficial to efficiently utilize sunlight of MIL-101(Fe).

Furthermore, XPS was conducted to determine the valence states and chemical composition of samples. The result of survey spectrum in Fig. 2f explicitly demonstrated the existence of elements C, Fe, O, and Ag, which is accordance with the EDX analysis. In C 1s spectra (Fig. 2g), the binding energies of 288.8 eV for carboxyl group and 284.7 eV belonged to terephthalic acid group were observed [32,33]. As depicted in Fig. 2h, the O 1s peaks at 532.0, 531.3 and 530.2 eV were derived from carboxylic acid group, Fe-O and H–O-H respectively [34]. From the Fe 2p spectra in Fig. 2i, the peaks at 725.1, 711.5 and 717.5 eV corresponded to Fe^{3+} [35]. In addition, two distinct peaks at 373.9 and 367.9 eV assigned to metallic Ag in Fig. 2j were observed [21], further demonstrating successful introduction of Ag NPs in the composite. Meantime, the mass ratio of Ag atoms in the composite was investigated and depicted in Table S1 (Supporting information), it is noteworthy that the mass ratio of Ag atoms is not as much as expected, which may ascribe to the incomplete deposition of Ag nanoparticles during the photo-deposition process.

The catalytic activities of as-synthesized catalysts over different systems were studied and illustrated in Fig. 3a. BPA showed negligible self-degradation. By the PMS alone, MIL-101(Fe) merely degraded 7% of BPA, implying its sluggish PMS activation ability. Comparatively, the BPA degradation was slightly improved (∼13%) by Ag/MIL-101(Fe), originating from the PMS activation ability of metallic Ag [21]. For the photocatalytic process, nearly 21% of BPA was degraded over MIL-101(Fe) upon light irradiation, which due to its poor photocatalytic activity resulting from the sluggish photoinduced charge carrier separation. Whereas, 51% of BPA was removed over Ag/MIL-101(Fe), indicating that loading of metallic silver effectively boosts photoinduced electron-holes separation thus improved photocatalytic activity. Notably, the addition of PMS strikingly accelerated the photocatalytic BPA degradation of Ag/MIL-101(Fe), nearly 100% of BPA was removed after 20 min. Previous studies demonstrated that the metallic Ag nanoparticles possessed chemical activating PMS ability [36,37]. Whereas, without light irradiation, only 13% of BPA can be degraded over Ag/MIL-

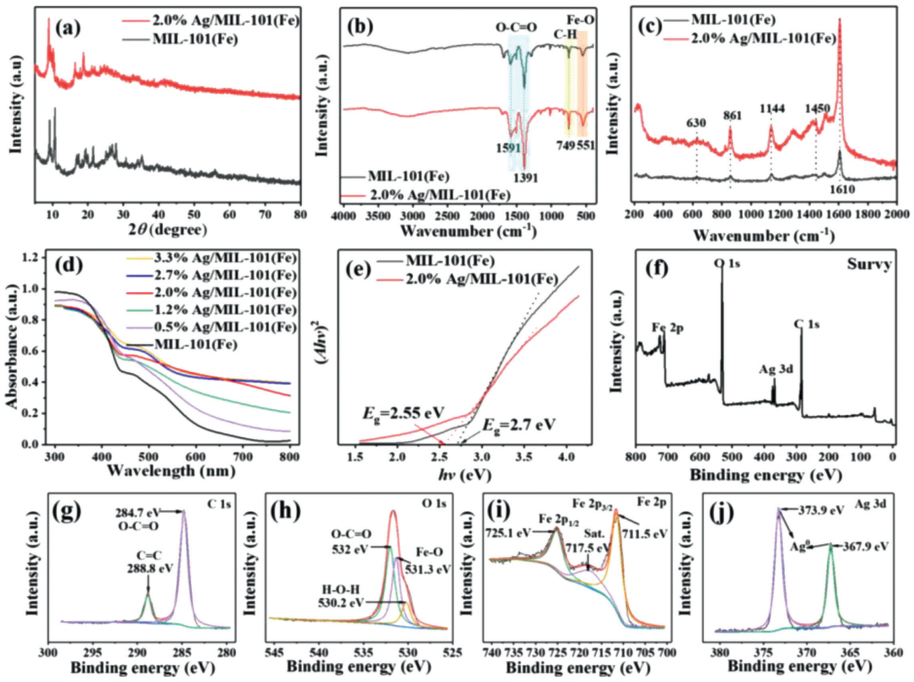

Fig. 2. (a) XRD spectrum, (b) FT-IR spectra, (c) Raman spectra, (d) UV–vis diffuse reflectance spectra and (e) Tauc Plot spectra of MIL-101(Fe) and Ag/ MIL-101(Fe). XPS spectra of Ag/MIL-101(Fe): (f) survey, (g) C 1s, (h) O 1s, (i) Fe 2p and (j) Ag 3d.

101(Fe)/PMS. These suggested that there existed a synergistic effect of metallic Ag NPs and MIL-101(Fe), which might be interpreted as the photoinduced electrons triggering PMS activation to produce more $SO_4^{\bullet-}$. It revealed that Ag/MIL-101(Fe) possessed remarkable photocatalytic PMS activation performance for BPA degradation. In addition, the catalytic performances of Ag/MIL-101(Fe) containing different contents of Ag in presence of PMS were studied. As depicted in Fig. 3b, all the composites presented enhanced photocatalytic performances, but the degradation process showed poor result with a pseudo-first-order kinetic model. This may be attributed to self-declined reaction rate of the PMS [38]. So, we adopted a retarded first-order model according to Eq. 1 [39], which could adequately describe the reaction trend (Figs. 3c and d).

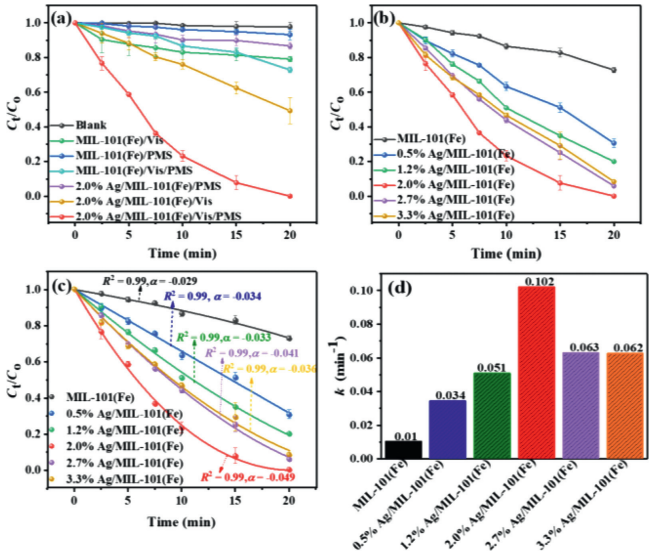

Fig. 3. Photocatalytic activities in BPA degradation over (a) different systems, (b) Ag/ MIL-101(Fe) with different contents of Ag. (c, d) The comparison of kinetic calculated corresponding k of different contents of Ag.

Among them, the optimized 2.0% Ag/MIL-101(Fe) sample possessed the best photocatalytic performance with kinetic constant (k) of 0.102 min^{-1}, almost 10-fold of pristine MIL-101(Fe). The above results indicate that introduction of Ag improved the photocatalytic activity of MIL-101(Fe) with PMS.

$$C_t = C_0(1+\alpha t)^{-k/\alpha} \quad (1)$$

where C_t and C_0 express the concentration of the BPA at initial and at time t (min), respectively. α is the "sliding factor" and k represents the apparent reaction rate (min^{-1}). Moreover, TOC were investigated in different systems including MIL-101(Fe)/PMS/Vis and Ag/MIL-101(Fe)/PMS/Vis, as shown in Fig. S3 (Supporting information). The TOC removal efficiency in the Ag/MIL-101(Fe)/PMS/Vis system was 84.7%, which was higher than that of MIL-101(Fe)/PMS/Vis (15.7%). This implies that excellent mineralization ability of the composite and more BPA are mineralized to CO_2 and H_2O.

The factors affecting the photocatalytic BPA degradation by Ag/MIL-101(Fe) catalyst were studied and shown in Fig. S1 (Supporting information). From Fig. S1a, the photocatalytic activity of the composite toward BPA removal increases gradually with increasing PMS concentration from 0.5 mmol/L to 1 mmol/L. Whereas, by adding PMS up to 3.0 mmol/L, the degradation efficiency was no further promoted. The main reason might be that excess PMS will consume the formed $SO_4^{\bullet-}$ to generate inactive $SO_5^{\bullet-}$ and $HO_2^{\bullet}$, which hinders the degradation process [40]. The impact of initial BPA concentration was showed in Fig. S1b. Obviously, the degradation rates tended to descend rapidly with BPA concentration increased. This may be attributed to the fact that the active sites were covered by the excess BPA in high concentration, therefore hindered the PMS activation. Moreover, the result in Fig. S1c indicated the increase of catalyst dosage accelerated removal of BPA. This is arising from the higher dosage could introduce more active sites for PMS to produce more active radicals. Fig. S1d disclosed the impact of initial pH on the reaction. The BPA removal efficiency deceased as the pH value from 7 up to 10. This implies that the generated active radicals in the system are more suitable for coexistence in acidic conditions [41]. In addition, anions are

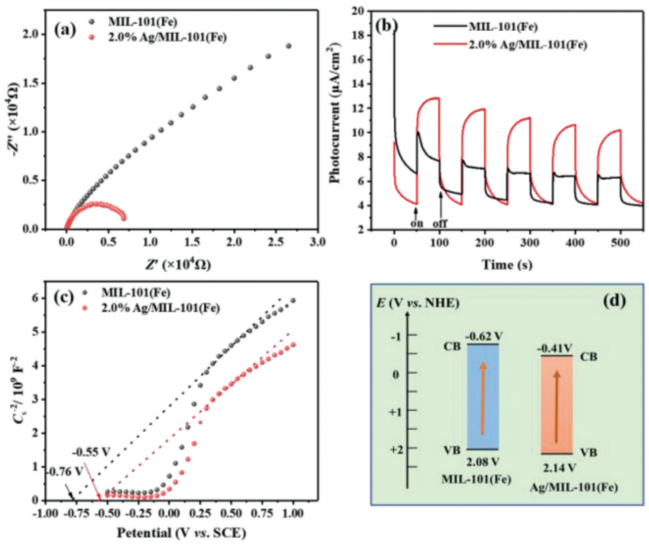

Fig. 4. (a) EIS Nyquist impedance plots, (b) transient photocurrent responses, (c) Mott-Schottky plot and (d) the band alignments of the MIL-101(Fe) and Ag/MIL-101(Fe).

also an essential factor during the reaction process. From Fig. S1e, $H_2PO_4^-$ and HCO_3^- inhibit the BPA removal, whereas Cl^- remarkably promotes the BPA degradation. In general, HCO_3^- can react with $^{\bullet}OH$ and $SO_4^{\bullet-}$ to yield weak oxidizing $HCO_3^{\bullet}$ [42]. $H_2PO_4^-$ often used as a chelating agent to quench free radicals through spatial isolation [43]. Thus, the HCO_3^- and $H_2PO_4^-$ showed inhibitory effects on BPA removal. Usually, according to Eqs. 2-4, Cl^- would quench $SO_4^{\bullet-}$ and $^{\bullet}OH$ to form $Cl^{\bullet}$ and $HOCl^{\bullet-}$ with relatively weak activity, respectively, which had a negative impact on the photocatalysis system [44]. However, it is worth noted that adding Cl^- to this reaction system can speed up the BPA degradation. This may originate from the active chlorine species ($HClO/Cl_2$) produced by the excess of Cl^-, which accelerate the degradation of BPA according to Eqs. 5 and 6 [45,46].

$$Cl^- + {}^{\bullet}OH \leftrightarrow HOCl^{\bullet-} \quad (2)$$

$$HOCl^{\bullet-} \leftrightarrow Cl^{\bullet} + HO_2 \quad (3)$$

$$Cl^- + SO_4^{\bullet-} \leftrightarrow SO_4^{2-} + Cl^{\bullet} \quad (4)$$

$$Cl^- + HSO_5^- \rightarrow SO_4^{2-} + HOCl \quad (5)$$

$$2Cl^- + HSO_5^- + H^- \rightarrow SO_4^{2-} + Cl_2 + HO_2 \quad (6)$$

In order to understand the contribution of Ag in the charge carrier transfer and separation behavior of the composite, the EIS, photo-chronoamperometry and Mott-Schottky (M-S) spectrum were studied. As depicted in Fig. 4a of the Nyquist plot of EIS spectrum, a distinct decrease of semicircle radius for Ag/MIL-101(Fe) composite is observed, manifesting that effective interfacial charge transfer and smaller charge transfer resistance of Ag/MIL-101(Fe) [47]. From Fig. 4b, the transient photocurrent response of the samples was recorded. Obviously, the Ag/MIL-101(Fe) presents a promoted photocurrent generation, indicating the promoted separation capability of charge carriers of Ag/MIL-101(Fe). Moreover, Fig. 4c illustrated the M-S curves of the catalysts. The observed positive slopes manifest the n-type property of two catalysts. Meantime, the flat band potential (E_{fb}) extrapolated for MIL-Fe and Ag/MIL-Fe are −0.76 and −0.55 V (*vs.* SCE), respectively, equivalent to −0.52 and −0.31 V (*vs.* NHE). It is most acceptable that the conduction band potential (E_{CB}) of n-type semiconductor is 0.1∼0.3 V above the V_{FB} [44]. Therefore, the E_{CB} of two catalysts locates at −0.62 and −0.41 V (*vs.* NHE), respectively. Apparently, the conduction potential of two catalysts is more negative than $SO_4^{\bullet-}/SO_4^{2-}$ (2.5–3.1 V) and $O_2/^{\bullet}O_2^-$ (0.16 V), which satisfies the thermodynamically reduction of PMS to yield $SO_4^{\bullet-}$ as well as reduce O_2 to generate $^{\bullet}O_2^-$, respectively [45]. Combining the calculated band-gap value (Fig. 2e), the valence band potentials (E_{VB}) for two catalysts are evaluated to 2.08 and 2.14 V respectively, which are inactive for oxidizing OH^- to $^{\bullet}OH$ (2.38 V *vs.* NHE). Thus, the band alignment of MIL-101(Fe) and Ag/MIL-101(Fe) was depicted in Fig. 4d.

To unveil the underlying mechanism of the reaction process, the involved active species produced in the reaction were firstly investigated through radical trapping experiments. In this study, different scavengers were applied to quench the formed radicals, including TBA for $^{\bullet}OH$, MeOH for both $SO_4^{\bullet-}$ and $^{\bullet}OH$, furfuryl alcohol (FFA) for $^1O_2$ and *p*-BQ for $^{\bullet}O_2^-$ [46]. The results in Figs. 5a and b illustrated that the degradation efficiencies of composite were obviously declined with adding different scavengers, suggesting that $SO_4^{\bullet-}$, $^{\bullet}OH$, $^{\bullet}O_2^-$ and $^1O_2$ are the major oxidized species in Ag/MIL-101 (Fe)/PMS/Vis system and play a vital role in this reaction.

Furthermore, to clarify the reactive species during the reaction process, ESR tests were performed. As depicted in Fig. 5c, for bare MIL-101(Fe), no obvious signal was observed in MIL-101(Fe)/PMS system, testifying to the poor PMS activation. By contrast, upon visible light irradiation, the typical $^{\bullet}OH$ ($a_N = a_H = 14.9$ G) and $SO_4^{\bullet-}$ ($a_N = 13.8$ G, $a_H = 10.1$ G, $a_H = 1.42$ G, $a_H = 0.8$ G) signals can be detected [48]. This manifested that visible-light can trigger MIL-101(Fe) to activate PMS. Meanwhile, the distinct $^{\bullet}OH$ and $SO_4^{\bullet-}$ signals were also observed in Ag modified MIL-101(Fe), implying the promoted PMS activation after Ag loading. More significantly, the $SO_4^{\bullet-}$ and $^{\bullet}OH$ signals in Ag/MIL-101(Fe)/PMS/Vis system are much stronger than that of Ag/MIL-101(Fe)/PMS system, demonstrating that illumination accelerated PMS activation of the composite. Notably, the $^{\bullet}OH$ signal intensity was directly related to $SO_4^{\bullet-}$, which originated from the reaction of H_2O/OH^- and generated $SO_4^{\bullet-}$ [49]. Fig. 5d showed that the obvious $^{\bullet}O_2^-$ signal were found in Ag/MIL-101(Fe)/PMS/Vis and MIL-101(Fe)/PMS/Vis system. It is noteworthy that the signal of $^{\bullet}O_2^-$ became weaker after Ag loading, which might be due to the consumption of $^{\bullet}O_2^-$ by other reactions. From Fig. 5e, a typical TEMP-$^1O_2$ signal with the 1:1:1 triplet characteristic was clearly observed in Ag/MIL-101(Fe)/PMS. From previous researches [50,51], the reaction between $^{\bullet}O_2^-$ and other radicals can lead to $^1O_2$ generation, thus result in the weak signal of $^{\bullet}O_2^-$ in Ag/MIL-101(Fe)/PMS/Vis. In brief, the above studies revealed that the active $SO_4^{\bullet-}$, $^{\bullet}OH$, $^{\bullet}O_2^-$ and $^1O_2$ were engaged in BPA degrading.

The possible degradation pathways of BPA in the Ag/MIL-101(Fe)/PMS/Vis system were analyzed by DFT calculation and HPLC-MS analysis. Three potential degradation pathways are suggested base on the observed intermediates in Table S2 and Fig. S2 (Supporting information). The ROS produced in this study ($SO_4^{\bullet-}$, $^{\bullet}OH$, $^{\bullet}O_2^-$ and $^1O_2$) are widely regarded as electrophilic species [52], thus the calculated values of condensed Fukui index (f^-) was adopted to predict the reaction sites of BPA molecules. The chemical structure of BPA and isosurface of electron density of the f^- on BPA were depicted in Figs. 6a and b, respectively. f^- representing electrophilic attack was calculated and shown in Fig. 6c. It is found C4(C11), C9(C16), C7(C14) have the highest f^- values, indicating that they are the most reactive sites for radical attacks. The possible degradation pathways of BPA were shown in Fig. 6d. Firstly, BPA molecules undergo hydroxylation process, $^{\bullet}OH$ prefer to attack on C9(C16), resulting in **P1** ($m/z = 243$) formation. Then **P1** undergo β-scission to form intermediate **P2** and **P3** free radicals. **P4** ($m/z = 168$) can be obtained by the reaction of **P2** and $^{\bullet}OH$. And **P3** accepts H^+ to form phenol molecules ($m/z = 93$) [53]. The C4(C11) site of BPA molecule is also vulnerable to electrophilic attack to

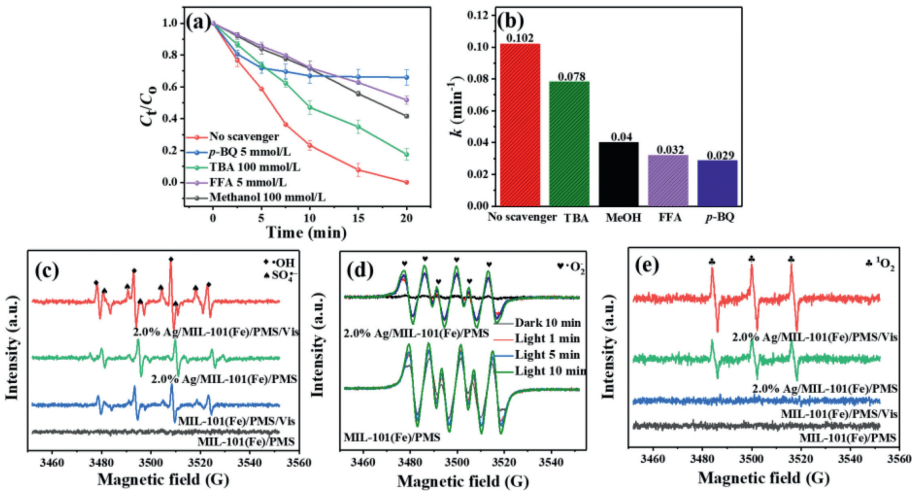

Fig. 5. (a) Radical species trapping experiments and (b) the corresponding reaction constants of Ag/MIL-101(Fe)/PMS/Vis system; ESR signals of (c) DMPO-$SO_4^{\bullet-}$, DMPO-$^{\bullet}OH$, (d) DMPO-$^{\bullet}O_2^-$ and (e) TEMP-$^1O_2$ in the various photocatalytic systems.

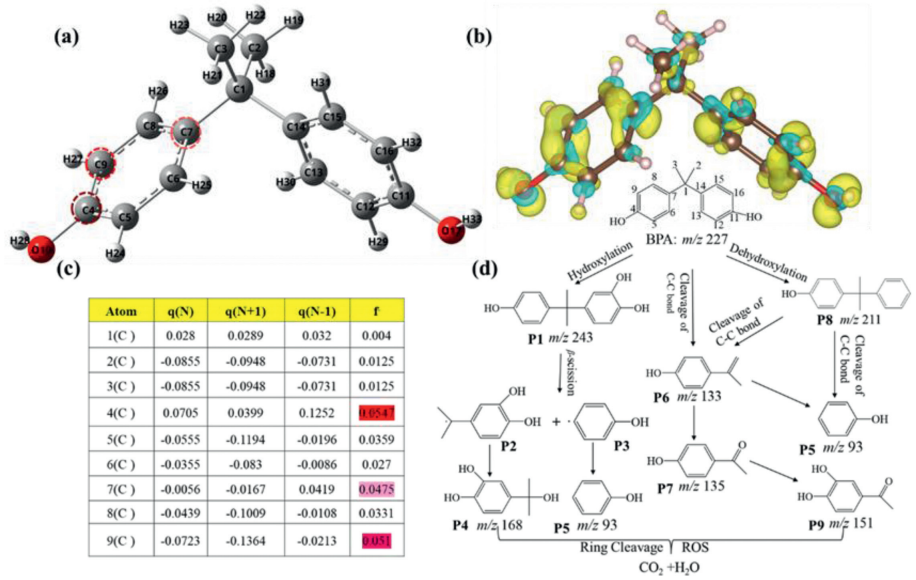

Atom	q(N)	q(N+1)	q(N-1)	f
1(C)	0.028	0.0289	0.032	0.004
2(C)	-0.0855	-0.0948	-0.0731	0.0125
3(C)	-0.0855	-0.0948	-0.0731	0.0125
4(C)	0.0705	0.0399	0.1252	0.0547
5(C)	-0.0555	-0.1194	-0.0196	0.0359
6(C)	-0.0355	-0.083	-0.0086	0.027
7(C)	-0.0056	-0.0167	0.0419	0.0475
8(C)	-0.0439	-0.1009	-0.0108	0.0331
9(C)	-0.0723	-0.1364	-0.0213	0.051

Fig. 6. (a) BPA chemical structure, (b) isosurface of electron density of the Fukui index (f^-) on BPA (isosurface value = 0.003), (c) condensed f^- value for each atom calculated using the Hirschfeld charge, (d) proposed BPA degradation pathways in the Ag/MIL-101(Fe)/PMS/Vis system.

form **P8** ($m/z = 211$). The electron-rich groups in **P8** were attacked by the activated species to generate **P6** ($m/z = 133$). The C–C bond in **P6** was attacked and form **P5** phenol molecules ($m/z = 93$). In addition, due to the high f^- value of C7(C14) site of BPA molecule, the C–C bond may directly cleavage to generate **P6** ($m/z = 133$), and then further hydroxylation to form generates **P9** ($m/z = 151$). Finally, all intermediate products were oxidized into carbon dioxide and water.

The durability of composite during photocatalytic reaction was also analyzed. Fig. S4a (Supporting information) revealed that the degradation efficiency of BPA slowly declined after four cycle tests, which might due to the loss of silver nanoparticles after four cycles. However, the degradation efficiency stills maintained a level above 72%. The TEM images (Fig. S4b in Supporting information) showed that the used catalyst retained a similar morphology of the pristine composite. From the XPS spectrum of the used Ag/MIL-101(Fe), the peak of Fe^{2+} was found (Fig. S4c in Supporting information), which indicated that part of Fe^{3+} transformed to Fe^{2+} due to electron transfer in the reaction [54]. Moreover, two peaks assigned to the metallic Ag can be observed, indicating the valence state of silver was unchanged. This demonstrates that the Ag/MIL-101(Fe) composite kept relatively stable structure.

On the base of the above analysis, a tentative photocatalytic mechanism for the outstanding performance of Ag/MIL-101(Fe) composite with PMS is proposed (Fig. 7). Upon photoexcitation, both MIL-101(Fe) and Ag nanoparticles are simultaneously excited. The Ag nanoparticles can extract photoinduced electrons from MIL-101(Fe) by the formed junction, which promotes the photoinduced charge carrier separation of MIL-101(Fe). The hot electrons generated in Ag by SPR effect with high reduction power can reduce the adsorbed PMS to generate $SO_4^{\bullet-}$, or O_2 to produce $^{\bullet}O_2^-$. Meantime, the reaction between the adsorbed H_2O/OH^- and $SO_4^{\bullet-}$ yielded $^{\bullet}OH$ [55]. On the other side, the photoinduced electron (e^-) of MIL-101(Fe) are captured by adsorbed O_2 to yield $^{\bullet}O_2^-$, and then $^{\bullet}O_2^-$ recombined with h^+ for $^1O_2$ generation [56]. Moreover, the metallic Ag can also trigger PMS activation to produce $SO_4^{\bullet-}$ or $^1O_2$. Finally, all the formed active radicals participate in the decomposition of BPA.

In conclusion, a plasmonic Ag NPs decorated MIL-101(Fe) hybrid was prepared *via* a photo-deposition method. Upon illumi-

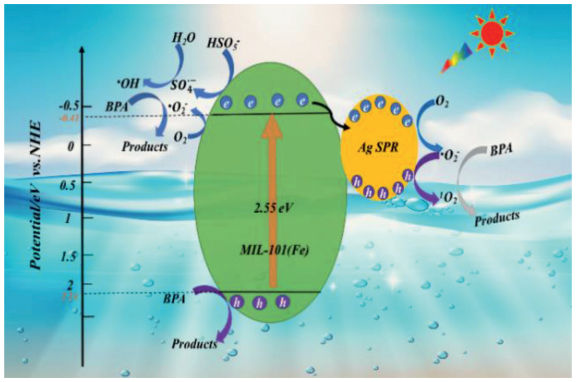

Fig. 7. The possible photocatalytic mechanism of degradation.

nation, the composites displayed superior photocatalytic activities for BPA removal. Almost 100% of BPA was degraded over the optimized composite and the catalytic activity promoted up to 10-fold of pristine MIL-101(Fe). The experiment results demonstrated that the introduction of plasmonic Ag facilitate the photo-induced carrier separation, broaden light-response range, and accelerate PMS activation of MIL-101(Fe). During the photocatalytic PMS activation, BPA was removed by the formed $^{\bullet}OH$,$SO_4^{\bullet-}$, $^{\bullet}O_2^-$ and $^1O_2$. This study will pave a new way in developing highly-efficient photocatalyst with excellent PMS activation ability for waste water treatment.

Declaration of competing interest

The authors declare that they have no known competing financial interests or personal relationships that could have appeared to influence the work reported in this paper.

Acknowledgements

This work was financially supported by Natural Science Foundation of Hebei Province, China (No. B2020202044), and the Open Foundation of Key Laboratory of Industrial Ecology and Environmental Engineering, MOE, China (No. KLIEEE-21–04).

References

[1] B. Yilmaz, H. Terekeci, S. Sandal, et al., Rev. Endocr. Metab. Dis. 21 (2020) 127–147.
[2] L.N. Vandenberg, M.V. Maffini, C. Sonnenschein, et al., Endocr. Rev. 30 (2009) 75–95.
[3] A. Svenson, A.S. Allard, M. Ek, Water Res. 37 (2003) 4433–4443.
[4] Z. Fang, P. Chelme-Ayala, Q. Shi, et al., Chemosphere 211 (2018) 271–277.
[5] A. Ledjeri, I. Yahiaoui, F. Aissani-Benissad, et al., J. Environ. Manage. 184 (2016) 249–254.
[6] O.S. Furman, A.L. Teel, R.J. Watts, Environ. Sci. Technol. 44 (2010) 6423–6428.
[7] T. Garoma, S. Matsumoto, Y. Wu, et al., Ozone Sci. Eng. 32 (2010) 338–343.
[8] R.A. Torres, C. Pétrier, E. Combet, et al., Ultrason. Sonochem. 15 (2008) 605–611.
[9] X. Chen, J. Yao, H. Dong, et al., Water Res. 207 (2021) 117800.
[10] J. Du, B. Zhang, J. Li, B. Lai, Chin. Chem. Lett. 31 (2020) 2575–2582.
[11] J. Duan, L. Chen, H. Ji, et al., Chin. Chem. Lett. 33 (2022) 3172–3176.
[12] M. Eddaoudi, J. Kim, N. Rosi, et al., Science 295 (2002) 469–472.
[13] S.K. Henninger, H.A. Habib, C. Janiak, J. Am. Chem. Soc. 131 (2009) 2776–2777.
[14] A. Car, C. Stropnik, K.V. Peinemann, Desalination 200 (2006) 424–426.
[15] J.S. Wang, X.H. Yi, X. Xu, et al., Chem. Eng. J. 431 (2022) 133213.
[16] X. Li, W. Guo, Z. Liu, et al., Chem. Eng. J. 324 (2017) 665–672.
[17] X.H. Yi, H. Ji, C.C. Wang, et al., Appl. Catal. B: Environ. 293 (2021) 120229.
[18] Y. Jiang, Z. Wang, J. Huang, et al., Chem. Eng. J. 439 (2022) 135788.
[19] S. Linic, P. Christopher, D.B. Ingram, Nat. Mater. 10 (2011) 911–921.
[20] C. Wang, D. Astruc, Chem. Soc. Rev. 43 (2014) 7188–7216.
[21] S. Ghattavi, A. Nezamzadeh-Ejhieh, Mater. Res. Bull. 158 (2023) 112085.
[22] Z. Ren, F. Chen, K. Wen, et al., J. Photoch. Photobiol. A 389 (2020) 112217.
[23] W. Li, W. Qi, L. Cai, et al., Chem. Phys. Lett. 738 (2020) 136873.
[24] H. Liang, R. Liu, X. An, et al., Chem. Eng. J. 414 (2021) 128669.
[25] C. Zhao, P. Dong, Z. Liu, et al., RSC Adv. 7 (2017) 24453–24461.
[26] J. Tang, M. Yang, M. Yang, et al., New J. Chem. 39 (2015) 4919–4923.
[27] H. Liang, R. Liu, C. Hu, et al., J. Hazard Mater. 406 (2021) 124692.
[28] Y. Liu, Y. Xie, M. Dai, et al., Materials (Basel) 12 (2019) 1453.
[29] S. Bordiga, C. Lamberti, G. Ricchiardi, et al., Chem. Commun. 20 (2004) 2300–2301.
[30] K. Tan, N. Nijem, P. Canepa, et al., Chem. Mater. 24 (2012) 3153–3167.
[31] Y. Lin, C.E. Bunker, K.S. Fernando, et al., ACS Appl. Mater. Interfaces 4 (2012) 1110–1117.
[32] X. Zhang, Y. Yang, W. Huang, et al., Mater. Res. Bull. 99 (2018) 349–358.
[33] W. Huang, C. Jing, X. Zhang, et al., Chem. Eng. J. 349 (2018) 603–612.
[34] W. Zhang, Y. Sun, J. Li, et al., J. Catal. 357 (2018) 41–50.
[35] X.Q. Tang, Y.D. Zhang, Z.W. Jiang, et al., Talanta 179 (2018) 43–50.
[36] Y.Y. Ahn, E.T. Yun, J.W. Seo, et al., Environ. Sci. Technol. 50 (2016) 10187–10197.
[37] K. Shoueir, A. Mohanty, I. Janowska, J. Clean. Prod. 351 (2022) 131540.
[38] J. Ma, L. Chen, Y. Liu, et al., J. Hazard Mater. 418 (2021) 126180.
[39] J. Duan, H. Ji, T. Xu, et al., Chem. Eng. J. 406 (2021) 126752.
[40] C.X. Li, C.B. Chen, J.Y. Lu, et al., Chem. Eng. J. 337 (2018) 101–109.
[41] K. Zhang, D. Sun, C. Ma, et al., Chemosphere 241 (2020) 125021.
[42] J. Ma, Y. Yang, X. Jiang, et al., Chemosphere 190 (2018) 296–306.
[43] A. Ghauch, A.M. Tuqan, Chem. Eng. J. 183 (2012) 162–171.
[44] N. Liu, W. Huang, X. Zhang, et al., Appl. Catal. B: Environ. 221 (2018) 119–128.
[45] C. Tang, E. Liu, J. Fan, et al., Rsc. Adv. 5 (2015) 91979–91987.
[46] Y. Gao, Y. Zhu, L. Lyu, et al., Environ. Sci. Technol. 52 (2018) 14371–14380.
[47] Y.C. Zhou, P. Wang, H. Fu, et al., Chin. Chem. Lett. 31 (2020) 2645–2650.
[48] L. Chen, J. Duan, P. Du, et al., Water Res. 221 (2022) 118747.
[49] Y. Gong, B. Yang, H. Zhang, et al., J. Mater. Chem. A 6 (2018) 23703–23711.
[50] C. Chen, L. Liu, Y. Li, et al., Chem. Eng. J. 384 (2020) 123257.
[51] Y. Li, J. Li, Y. Pan, et al., Chem. Eng. J. 384 (2020) 123361.
[52] J.Q. Li, Z.W. Zhou, X. Li, et al., Chem. Eng. J. 428 (2022) 132613.
[53] D. Roy, S. Neogi, S. De, Chem. Eng. J. 428 (2022) 131028.
[54] X. Wang, X. Pu, Y. Yuan, et al., Chin. Chem. Lett. 31 (2020) 2634–2640.
[55] X. Qiu, S. Yang, M. Dzakpasu, et al., Appl. Catal. B: Environ. 372 (2019) 605–615.
[56] Q. Zhao, C.C. Wang, P. Wang, Chin. Chem. Lett. 33 (2022) 4828–4833.